PAPER

Propulsion optimization of a jellyfish-inspired robot based on a nonintrusive reduced-order model with proper orthogonal decomposition

View the article online for updates and enhancements.

Bioinspiration & Biomimetics

PAPER

Propulsion optimization of a jellyfish-inspired robot based on a nonintrusive reduced-order model with proper orthogonal decomposition

Zixiang Ying[1] ![ORCID], Haozhi Zhang[1], Linxiang Wang[1,*] and Roderick Melnik[2]

1 State Key Laboratory of Fluid Power and Mechatronic Systems, Zhejiang University, 310027 Hangzhou, People's Republic of China
2 MS2Discovery Interdisciplinary Research Institute, Wilfrid Laurier University, Waterloo, ON N2L 3L5, Canada
* Author to whom any correspondence should be addressed.

E-mail: wanglx236@zju.edu.cn

Abstract

In this research, the propulsion of the proposed jellyfish-inspired mantle undulated propulsion robot (MUPRo) is optimized. To reliably predict the hydrodynamic forces acting on the robot, the proposed nonintrusive reduced-order model (NIROM) based on proper orthogonal decomposition (POD) additionally considers the POD basis that makes an important contribution to the features on the specified boundary. The proposed model establishes a mapping between the parameter-driven motion of the mantle and the evolution of the fluid characteristics around the swimmer. Moreover, to predict new cases where the input needs to be updated, the input of the proposed model is taken from the kinematics of the robot rather than extracted from full-order high-fidelity models. In this paper, it takes approximately 950 s to perform a simulation using the full-order high-fidelity model. However, the computational cost for one prediction with the proposed POD-NIROM is around 0.54 s, of which about 0.2 s is contributed by preprocessing. Compared with the NIROM based on the classic POD method, the proposed POD-NIROM can effectively update the input and reasonably predict the characteristics on the boundary. The analysis of the hydrodynamic performance of the MUPRo pinpoints that, over a certain period and with a certain undulation amplitude, the hydrodynamic force generated by the swinging-like mantle motion ($k < 0.5$) is greater, outperforming *Aequorea victoria* in startup acceleration. It is demonstrated that considering a certain power loss and a certain tail beat amplitude, the wave-like mantle motion ($k > 0.5$) can produce greater propulsion, which means higher propulsion efficiency.

1. Introduction

Recently, many scholars have sought inspiration from nature when designing underwater robots. Jellyfish vary in size from just a few millimeters to over 2 m long [1]. According to the fineness ratio, that is, the ratio of the axial length to the diameter of the jellyfish ($\tilde{H} = H/D$), jellyfish can be classified as prolate (when $\tilde{H} \geqslant 0.5$) or oblate (when $\tilde{H} < 0.5$) [2]. From the perspective of hydrodynamics, the above two types of jellyfish use different propulsion modes. Prolate jellyfish use jet propulsion and they generate almost all thrust during the contraction phase [3]. Oblate jellyfish generate propulsion like a rower. In

each swimming cycle, they can generate thrust during the contraction and relaxation phases [4].

In recent years, many creative ways have been proposed to propel a jellyfish-inspired robot. The research into prolate jellyfish-inspired robots has mainly focused on making better use of the instantaneous propulsion advantages of jet propulsion. For example, a jellyfish-inspired robot actuated by hydraulic networks [5], a robot inspired by jellyfish that utilizes ionic polymer-metal composite actuators as a routine propulsive means [6], a jet-propelled robot with an iris mechanism [7], a pulse jet robot that imitates the structure and swimming mode of a squid [8], an origami swimming robot using

jet propulsion [9]. In addition, some research has focused on designing a biomimetic robot that can be propelled like an oblate jellyfish. In particular, Robojelly [10] uses shape memory alloys to generate radial deformation of the artificial mantle for propulsion.

Oblate jellyfish using rowing propulsion can produce two peaks of propulsion in one swimming cycle [11]. Similarly, swimmers who use body/caudal fin (BCF) undulations also have two strokes in each swimming cycle (forward and backward tail strokes) [12]. It is worth mentioning that about 90% of fish use BCF propulsion [13], as this propulsion mode is widely used by underwater creatures. Considering that the prolate jellyfish has a more complete streamline and better orientation [14], it is sensible to design a robot in the shape of a prolate jellyfish and use mantle undulating as a propulsion mode.

For swimmers who use body waves for propulsion, their swimming performance largely depends on the characteristics of the reverse traveling wave (the body wave) on the body. Existing biological statistics [15, 16] and experimental results [17, 18] show that for a certain swimming speed, the swimmer's forward swimming efficiency mainly depends on the parameters of the body wave, such as undulating period (T), wavelength (k), and maximum lateral excursion (A_m). The propulsion produced by swimmers is an important indicator of their swimming efficiency. To evaluate the propulsion effect of the underwater robot and find the optimal value of its propulsion parameters, an efficient and fast model is needed to predict the hydrodynamic force received by the swimmer, taking the swimmer's current fluctuations (determined by body wave parameters) as input. The high-fidelity model used to obtain convincing simulation results requires the Navier–Stokes (N–S) equations to be solved for viscous fluids [19]. However, the intrinsic nonlinearity of these equations brings high computational costs, making rapid simulation a huge challenge. After decades of efforts to improve numerical methods, some more economical alternatives have been proposed. For example, the model reduction algorithm retains the main features of the solution state vector. Well-known methods for constructing reduced-order models (ROMs) include proper orthogonal decomposition (POD) [20–22], Koopman analysis [23] and dynamic mode decomposition [24–27].

POD is one of the earliest model reduction approaches applied in the field of fluid mechanics. It uses the POD modes (including the POD spatial model and the corresponding POD time coefficient) to build a reduced-dimensional model [28]. Recently, the POD method has been extensively used to solve a variety of problems in fluid dynamics [29–31]. In this article, the most important fluid feature is the wake vortex street generated by the swimmer's forward motion. The wake vortex originates from the separations of the boundary layer near the swimmer

[32]. Studies have shown that it is appropriate to use the POD method to extract the Karman vortex street characteristics of the wake [33–35]. This is an important reason for the POD method being selected in this article.

To quickly predict complex fluid dynamics phenomena, fast response and highly reliable methods are needed to capture the nonlinear dynamics of the fluid. In POD, performing Galerkin projection is the traditional method of building fluid dynamics models [36–38]. Thus, a ROM is constructed such that its computational cost is lower, compared with the full-order N–S equation. However, research has shown that some ROMs using Galerkin projection are unstable, even for canonical cases [39, 40]. At the same time, some POD-based nonintrusive ROMs (POD-NIROM) have been proposed and used for flow field prediction, which has outstanding performance in terms of model stability and nonlinear efficiency [20, 41].

Machine learning (ML) is a common method for POD-NIROM to treat complex turbulence problems. In fluid mechanics, ML has been widely used in data processing, data-driven control, and reduced-order modeling [42, 43]. In recent years, as a part of ML, deep learning algorithms [44] have been proved to be effective and potentially useful in the classification, regression, and feature recognition of fluid features, which can analyze and learn nonlinear and high-dimensional dynamic systems [45]. Meanwhile, studies have shown that the results obtained by the neural network (a hidden layer, a fully connected layer, and linear activation function) are equivalent to the results obtained by POD [46, 47]. As a kind of artificial neural network, long short-term memory neural networks (LSTM NNs) perform well in predicting or regressing time series data and have been successfully deployed in NIROM [48]. Meanwhile, studies have shown that the results obtained by the neural networks are similar to those obtained by POD [46].

Considering the potential in sequential data modeling, LSTM NNs have been used to construct ROMs of ocean circulation and flow around a cylinder [48, 49], which significantly reduces the computational cost. However, most existing ROMs for predicting the evolution of fluid characteristics still use sequences extracted from full-order systems as input. This brings a great computational cost in predicting new cases because the input also needs to be updated due to case changes. To this end, it has been shown that reducing the complexity of the equation governing the input can effectively increase the computational efficiency of the new cases prediction.

In the present research, the goal is to design a mantle undulated propulsion robot (named MUPRo) and optimize its propulsion parameters. In this regard, a POD-NIROM is proposed. Compared with the classic POD methods, the proposed model additionally considers the POD bases that have important

contributions to the characteristics on the specified boundary. On this basis, the proposed model can accurately predict the evolution of the fluid characteristics on the specified boundary which is used to calculate the instantaneous hydrodynamics acting on the robot. The proposed POD-NIROM is used to construct a mapping between the parameter-controlled mantle motion (that is, the boundary motion of the flow field) and the evolution of the fluid characteristics around the MUPRo (called the solution state vector). The existing fish kinematics is used to describe the mantle motion of MUPRo, from which some sinusoidal signals are extracted as the input of the proposed POD-NIROM, and then the LSTM NN is used to predict the evolution of fluid characteristics. Therefore, the proposed model can quickly update the input according to the new parameter combination, when predicting a new case. The computational efficiency of the proposed model is compared with the full-order HF model when predicting a large number of new cases. By comparing predictions and experiments, the reliability of POD-NIROM and the propulsion performance of the mantle under a variety of parameter combinations are discussed.

The rest of this article is organized as follows. The design of MUPRo and the proposed POD-NIROM are introduced in section 2. Section 3 introduces several important parameters for constructing the POD-NIROM. The evaluation of the proposed model and the discussion of propulsion performance of the mantle are presented in section 4.

2. Design and modeling of MUPRo

2.1. Bionic robot and its 2D prototype design

Inspired by jellyfish, the designed MUPRo utilizes the swimming performance of oblate jellyfish (that is, there are two propulsion peaks in each undulation period, as described in sections 3.1 and 4.4) and the good orientation of prolate jellyfish because of the symmetrical design and a more complete streamlined body [50–52]. Modular design is applied to the MUPRo of which mechanical structure is shown in figure 1(A). In addition to the control unit and the energy unit, the propulsion part is composed of several identical propulsion units. Each propulsion unit is composed of two parts, namely the drive mechanism (sealed in the main cabin) and the actuator (used to realize the undulation of the mantle). Similar to jellyfish, the geometry and mantle undulation of the MUPRo are rotationally symmetrical. This assumption is also applied to some dynamic simulations of the jellyfish-inspired robots [53, 54]. A numerical model (figure 1(B)) is present to simulate its swimming performance. The experimental design of the proposed 2D prototype is shown in figure 1(C). The ship-shaped block on the body axis is used to represent the cross section of the main

cabin, and the five-DOF multi-section bodies on the left and right sides are used to reproduce undulations of the mantle. As shown in figure 1(D), the 2D prototype is fixed on linear motion ball sliders. When the 2D prototype moves along the support, the resistance is negligible. The movement of the profile part along the support is completely restricted. Simultaneously, the displacement of the multi-segment body along the support is limited by the force sensor (figure 1(D)). The force sensor monitors the propulsion generated by the multi-segment body when imitating the mantle's undulating motion. The video of the 2D prototype experiment is presented in the supplementary material (https://stacks.iop.org/BB/17/046005/mmedia).

The length of the main cabin along the body axis of the MUPRo (that is, the length of the robot along the body axis, denoted by *BL*) is $BL = 672.48$ mm, and the width of the main cabin in the vertical body axis direction (denoted by *BW*) is $BW = 140$ mm. The mantle, which is rotationally symmetrical with respect to the body axis, is divided into five sections along the axial direction. The streamlined design is applied to the head of the main cabin (that is, the control unit), taking the NACA0030 airfoil as a reference. The mantle, which is rotationally symmetric with respect to the body axis, is divided into five sections along the axial direction. The mantle starts at $Xm_1 = 500$ mm, $Rm = 120$ mm, the width of the mantle $MW = 5$ mm and the length of each mantle section along the body axis is

$$[Lm_1, Lm_2, Lm_3, Lm_4, Lm_5]$$

$$= [100 \text{ mm}, 70 \text{ mm}, 70 \text{ mm}, 70 \text{ mm}, 70 \text{ mm}].$$
(1)

2.2. POD analysis of solution state vector

In fluid mechanics research, POD is widely used to extract the main features of the solution state vector $s(x, t, \theta)$, which includes the coherent structure [55] of the flow field. The solution state vector $s(x, t, \theta)$ is obtained by simulating the flow field around the MUPRo, whose mantle is periodically undulating. The computational domain and boundary conditions of the numerical model are shown in figure 1(B). The equations that govern the motion of Newtonian viscous fluids are the 2D incompressible N–S equations under arbitrary Lagrangian–Euler description,

$$\frac{\mathrm{d}u_i}{\mathrm{d}t} + \left(u_j - \frac{\mathrm{d}q_j}{\mathrm{d}t}\right)\frac{\partial u_i}{\partial x_j} = -\frac{\partial p}{\partial x_i} + \frac{\partial \tau_{ij}}{\partial x_j}, \quad (2)$$

$$\frac{\partial u_i}{\partial x_i} = 0, \quad (3)$$

where u_i is the flow velocity, τ_{ij} is the *ij* component of the viscous stress tensor, p is the pressure, x_i is the space coordinate, t is the time, and q_j is the grid displacement.
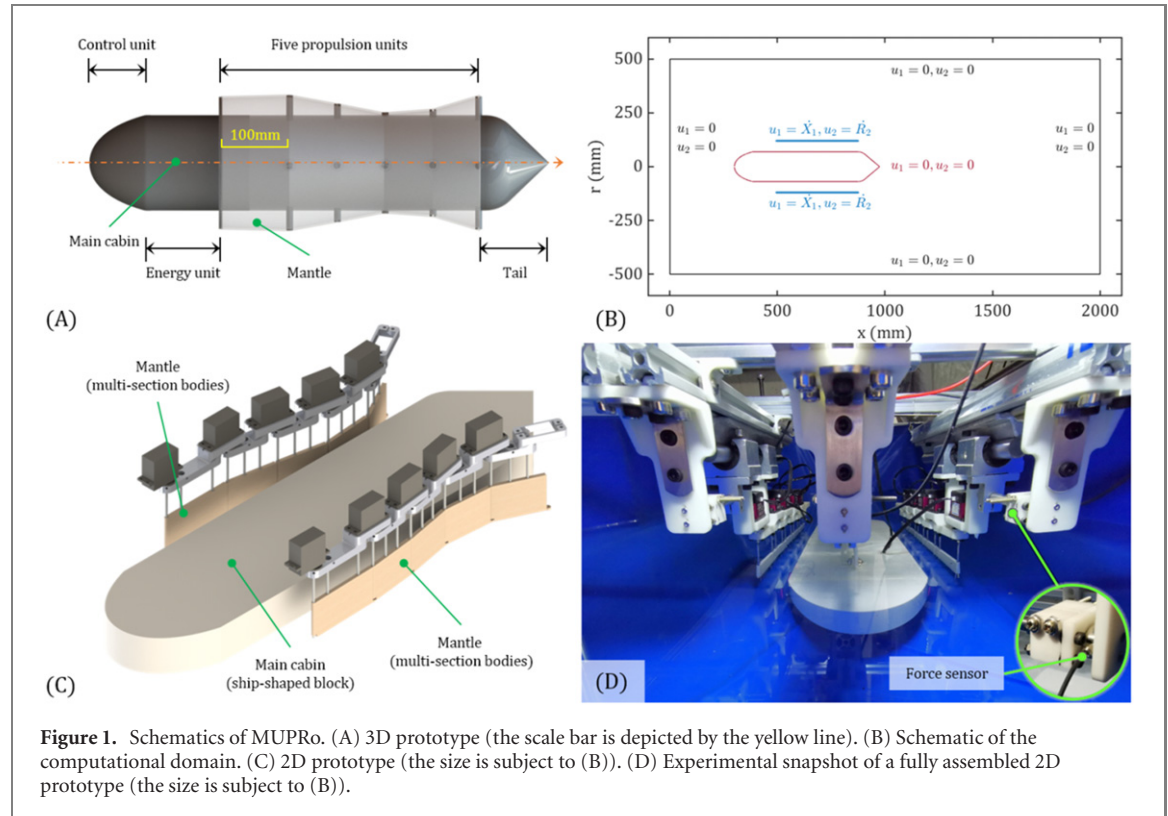
Figure 1. Schematics of MUPRo. (A) 3D prototype (the scale bar is depicted by the yellow line). (B) Schematic of the computational domain. (C) 2D prototype (the size is subject to (B)). (D) Experimental snapshot of a fully assembled 2D prototype (the size is subject to (B)).

Here, the movement of the mantle (the blue part of figure 1(B)) is specified with a known velocity of mantle $\dot{X}_{\mathrm{ma}} = \left[\dot{X}_i(t), \dot{R}_i(t)\right]$ (which describes the mantle motion derived from equation (10)). Therefore, the grid displacement of the entire computational domain $\dot{q}(t)$ can be obtained by solving the modified version of the Laplace grid movement algorithm [56]. The fractional step formulation is applied to the time dispersion of equation (2), and the specific process is described in detail in the existing literature [57–59]. As for the spatial discretization of the governing equations, the streamlined upwind Petrov–Galerkin finite element method is used to obtain a stable finite element solution [60, 61]. Studies have shown that the above algorithm is suitable for the simulation of the wake structures generated by the motion of upstream boundaries [62, 63], therefore, this method can be used to simulate the thrust generated by the reverse Karman street wake. The solution state vector $s(x, t, \theta)$ of equations (2) and (3) is given by the following formula:

$$s(x, t, \theta) = [s_1, s_2, s_3, s_4, s_5]^{\mathrm{T}} = \begin{bmatrix} q_x(x, t, \theta) \\ q_r(x, t, \theta) \\ u(x, t, \theta) \\ v(x, t, \theta) \\ p(x, t, \theta) \end{bmatrix}, \quad (4)$$

where $x = [x, r]$, the time is denoted by t, $q = (q_x, q_r)$ represents the mesh deformation field, $u = (u, v)$ is the velocity field, and p is the pressure field. By using Reynolds decomposition, ith solution state vector $s_i(x, t, \theta)$ can be expressed as follows,

$$s_i(x, t, \theta) = \langle s_i(x, t, \theta) \rangle + s_i'(x, t, \theta), \quad (5)$$

where $\langle s_i(x, t, \theta) \rangle$ represents the time average term and $s_i'(x, t, \theta)$ represents the fluctuating part. The fluctuating part $s_i'(x, t, \theta)$ is extracted as a linear combination of special modes $\Phi_j^{s_i}(x)$ and temporal modes $a_j^{s_i}(t)$, using the snapshot POD method [28, 34].

Thus, a few (represented by $r_\Omega^{s_i}$) sets of energy-favored spatial modes $\Phi_j^{s_i}$ can reproduce $s_i(x, t, \theta)$, combining with the corresponding temporal modes $a_j^{s_i}$,

$$s_i(x, t, \theta) \approx \langle s_i(x, t, \theta) \rangle + \sum_{j=1}^{r_\Omega^{s_i}} \Phi_j^{s_i}(x) \cdot a_j^{s_i}(t, \theta).$$

$$(6)$$

It is standard practice to estimate the total energy of ROM using eigenvalues [34, 64]. For simplicity, the total energy captured by POD-NIROM with $r^{s_i} = r_\Omega^{s_i} + r_{\Gamma_{\mathrm{m}}}^{s_i}$ POD modes is approximated by eigenvalues,

$$E_\Omega^{s_i} \approx \frac{\sum_{i=1}^{r^{s_i}} \lambda_i^{s_i}}{\sum_{i=1}^{n^{s_i}} \lambda_i^{s_i}}. \quad (7)$$

In the classic POD analysis (as described in equation (6)), some POD bases describing the characteristics of the fluid on the boundary are often discarded due to their insignificant contribution to the total energy. However, in this study, special attention is paid to the fluid characteristics on the boundary (especially the boundary corresponding to the mantle, denoted by Γ_{m}). In the proposed POD-NIROM, several (represented by $r_{\Gamma_{\mathrm{m}}}^{s_i}$) sets of the POD bases with dominant fluid characteristics on Γ_{m} are also

retained. The relative value of the captured fluid characteristics on the boundary of the jth POD base $\boldsymbol{\Phi}_j^{s_i}$ is defined as follows:

$$E_\Gamma^{s_i} = \frac{\int_{\Gamma_m} \left(\boldsymbol{\Phi}_l^{s_i}\right)^2 d\Gamma_m}{\sum_j^{n_{s_i}} \int_{\Gamma_m} \left(\boldsymbol{\Phi}_j^{s_i}\right)^2 d\Gamma_m} \quad (l \in r_{\Gamma_m}^{s_i}) \qquad (8)$$

where $n^{s_i} = n_t \times n_\theta$ is the number of snapshots, n_θ is the combinatorial number of the parameter space and each combination contains n_t snapshots.

In summary, in the proposed POD-NIROM, the fluctuating part of the solution state vector $s_i'(\boldsymbol{x}, t, \boldsymbol{\theta})$ is described by $r_{\Gamma_m}^{s_i}$ sets of POD bases dominated by boundary features and $r_\Omega^{s_i}$ sets of POD bases dominated by total energy:

$$s_i(\boldsymbol{x}, t, \boldsymbol{\theta}) \approx \langle s_i(\boldsymbol{x}, t, \boldsymbol{\theta}) \rangle + \sum_{j=1}^{r_\Omega^{s_i}} \boldsymbol{\Phi}_j^{s_i}(\boldsymbol{x}) \cdot a_j^{s_i}(t, \boldsymbol{\theta})$$

$$+ \sum_{l=1}^{r_{\Gamma_m}^{s_i}} \boldsymbol{\Phi}_l^{s_i}(\boldsymbol{x}) \cdot a_l^{s_i}(t, \boldsymbol{\theta}). \qquad (9)$$

2.3. Robot mantle kinematics

The main idea of the 2D prototype bionic propulsion is to drive the two multi-segment bodies on the side to imitate the same locomotion as a real oblate jellyfish. The backward traveling waves described by the Fourier series are used to describe the motion of the mantle [12, 65, 66]. For simplicity, the first term of the Fourier series is used to describe the lateral undulations of the body $\boldsymbol{R}_{ma}(x, t)$,

$$\boldsymbol{R}_{ma}(x, t) = A(x) \sin(2\pi kx - \sigma t), \qquad (10)$$

where $\boldsymbol{R}_{ma}(x, t)$ is the lateral (radial) excursion (along the R-axis), $A(x)$ is the first Fourier coefficient defining the maximum lateral displacement, k is the dimensionless wavenumber, $\sigma = 2\pi/T$ is the angular frequency, T is the undulating period. The envelope $A(x)$ can be approximated as a polynomial,

$$A(x) = A_0 + A_1 x + A_2 x^2, \qquad (11)$$

with the coefficients $A_0 = 0$, $A_1 = 0.1$ and $A_2 = 0$. The amplitude of the mantle undulation increases linearly from the start ($A = 0$) to the end ($A = 0.1ML$, ML is the mantle length). For reference, the average change in cross-sectional width of *Aequorea victoria* (a kind of oblate jellyfish) increased nonlinearly along the body axis with the greatest contraction (30%) at the margin [67]. The numerical approximation method is used to realize that each joint of the mantle in the 2D prototype fits on the body wave described by equation (10). In the following sections, the parameter that needs to be optimized is not only k. For intuitiveness, the parameter space $\boldsymbol{\theta}(k, T)$ is defined, which is composed of the dimensionless wave number k, and the period T.

2.4. LSTM NN-based POD-NIROM methodology

The LSTM network is used to construct a NIROM for the prediction of the pulsation of the solution state vector. The structure of the proposed method is shown in figure 2. It is divided into five branches (represented by different lines). The main idea of the 2D experimental branch (orange line with arrow) is to monitor the propulsion force $F_{exm}(\boldsymbol{x}, t, \boldsymbol{\theta})$ generated by the mantle undulation $\boldsymbol{X}_{ma}(t, \boldsymbol{\theta})$ under varied combinations of parameters. Similarly, the main purpose of the high-fidelity model branch (green line with arrow) is to calculate $F_{HF}(\boldsymbol{x}, t, \boldsymbol{\theta})$ and the solution state vector $s(\boldsymbol{x}, t, \boldsymbol{\theta})$. The NIROM prediction branch (blue line with arrow) is dedicated to predicting $F_{prd}(\boldsymbol{x}, t, \boldsymbol{\theta})$. Simply put, the prediction is mainly undertaken by the LSTM layer, and the fully connected layer downstream of the LSTM layer is used to convert the output $h(t, \boldsymbol{\theta})$ into the predicted temporal modes $\tilde{a}_j^{s_i}$. Other calculation branches (black lines with arrows) include the module that maps the parameter space $\boldsymbol{\theta}(k, T)$ to the mantle motion $\boldsymbol{X}_{ma}(t, \boldsymbol{\theta})$ (the mapping of equation (10)) and the module that decomposes the solution state vector $s(\boldsymbol{x}, t, \boldsymbol{\theta})$ into POD bases $\left[\boldsymbol{\Phi}_r^{s_i}(\boldsymbol{x}), \tilde{a}_r^{s_i}(t, \boldsymbol{\theta})\right]$ (the decomposition of equations (5) and (6)). The last one, the model training branch (dashed line with arrows) is used to train the NIROM (taking $x(t, \boldsymbol{\theta})$, which is the normalization of $\boldsymbol{X}_{ma}(t, \boldsymbol{\theta})$, as the input and $\tilde{a}_r^{s_i}(t, \boldsymbol{\theta})$ as the output).

LSTM was proposed by Hochreiter and Schmidhuber as early as 1997 [69]. The LSTM neural network (LSTM NN) is a recurrent neural network that is used to learn the sequential data (such as the data collected by sensors or probes) [70].

3. Analysis of POD-NIROM parameters

In what follows, MUPRo's swimming performance is of primary concern. POD-NIROM is constructed to find the parameters that lead the MUPRo to the most advanced state. Based on the solution state vector simulated from the HF model (introduced in the previous section), the data-driven model is constructed. Furthermore, to discuss the reliability of the solution state vector $s(\boldsymbol{x}, t, \boldsymbol{\theta})$, comparisons between experiments and simulations are carried out.

3.1. Validation study of the solution state vector

In this part, some cases are used to verify the solution state vector. In the experiment, the hydrodynamic force F_{exm} acting on the mantle (the one marked with the force sensor in figure 1(D)) along the body-axis (used for propulsion) generated by the mantle undulation can be directly collected by the force sensor. In the simulation, the mentioned propulsion force (represented by F_{HF}) is obtained by processing the solution state vector $s(\boldsymbol{x}, t, \boldsymbol{\theta})$ as follows:
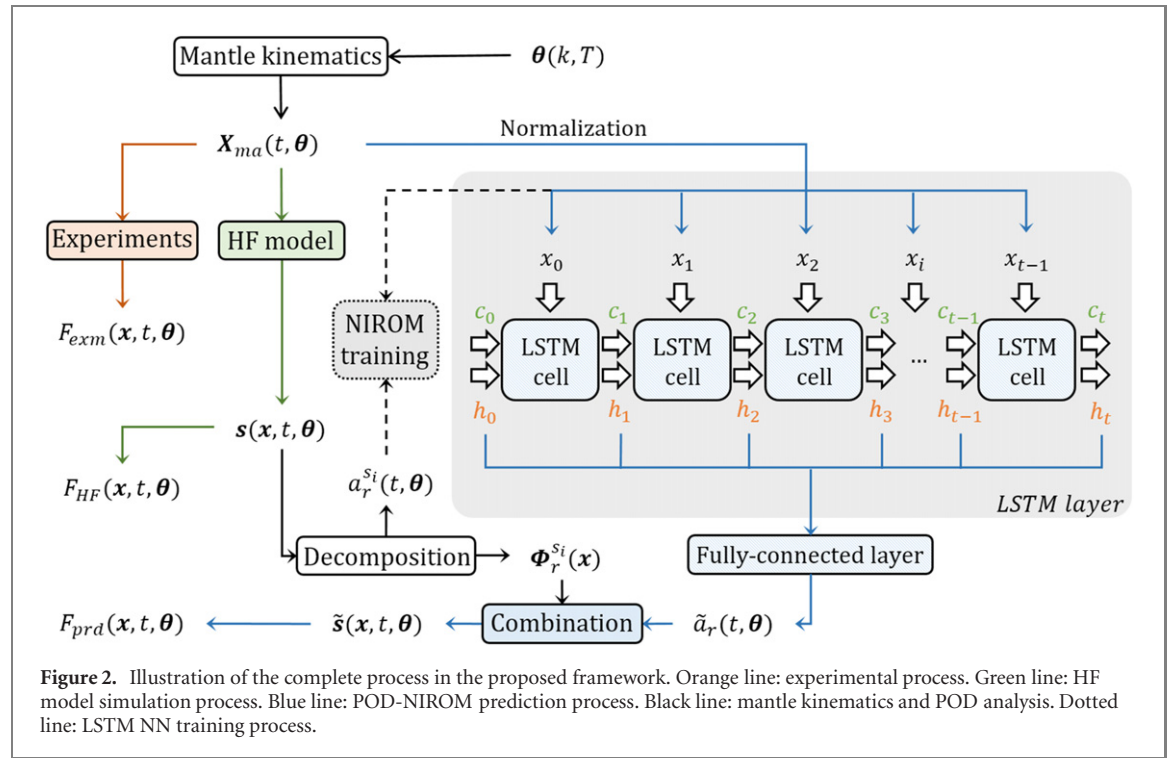
Figure 2. Illustration of the complete process in the proposed framework. Orange line: experimental process. Green line: HF model simulation process. Blue line: POD-NIROM prediction process. Black line: mantle kinematics and POD analysis. Dotted line: LSTM NN training process.

$$F_{\mathrm{HF}}(t) = \int_{\Gamma_{\mathrm{m}}} \left(-pn_x + \tau_{xx}n_x + \tau_{xr}n_r \right) \mathrm{d}\Gamma_{\mathrm{m}}, \quad (12)$$
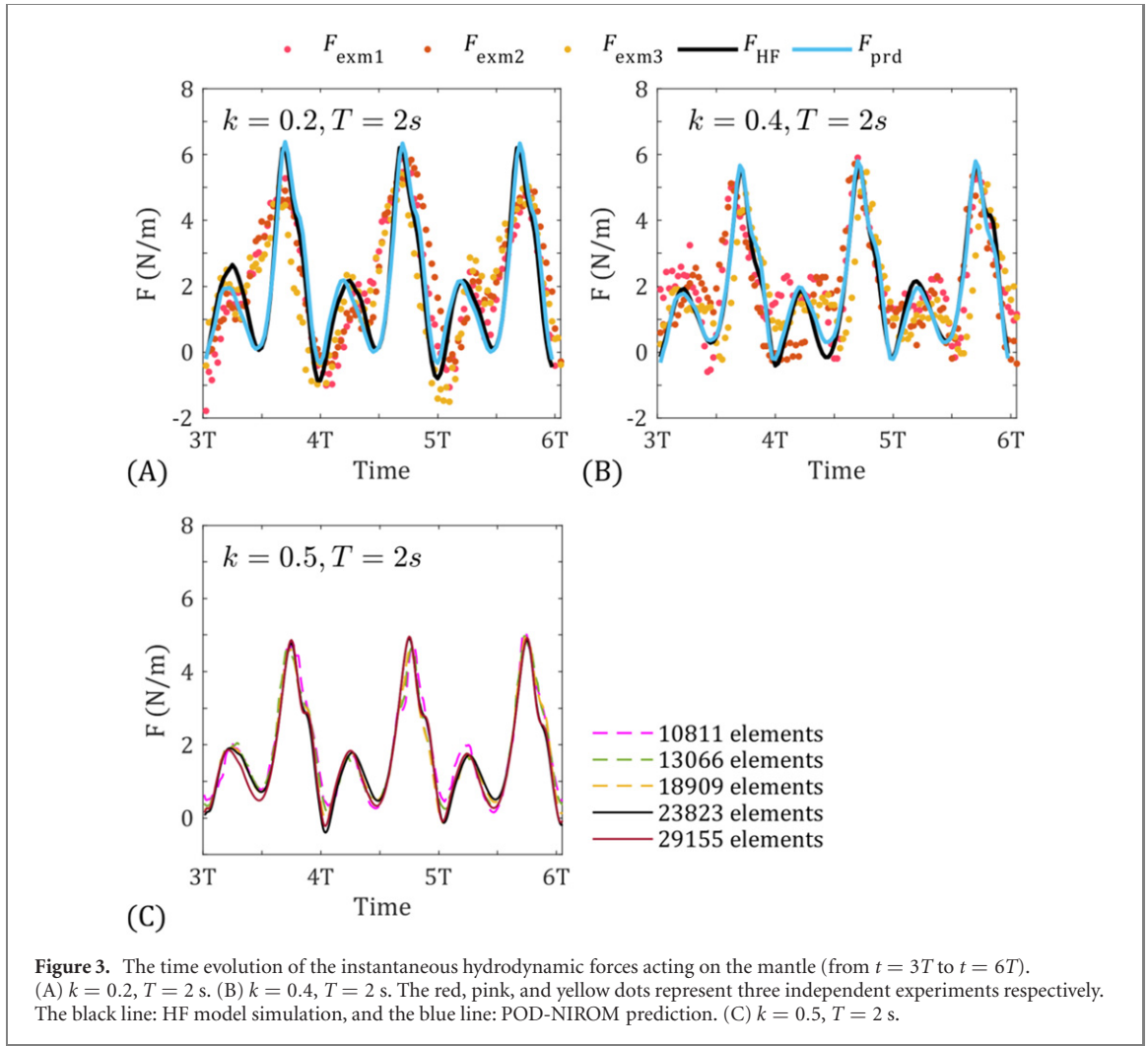
where $[n_x, n_r]^{\mathrm{T}}$ is the unit normal vector on the mantle boundary Γ_{m}. Figure 3 shows a comparison of the time series of the hydrodynamic forces (with positive thrust and negative resistance) acting on the mantle. Two peaks of propulsion force can be observed in each swimming cycle, which corresponds to forward and backward tail strokes [68]. However, the magnitude of the two propulsion peaks in one swimming cycle is different. This phenomenon is consistent with existing experimental research on the hydrodynamics of robots inspired by jellyfish [5]. In a swimming cycle, the larger propulsion peak occurs when the end of the mantle is at the position closest to the main cabin ($t = 0.75T + nT, n = 0, 1, 2 \ldots$). At the same time, when a small propulsion peak appears, the end of the mantle is farthest from the cabin ($t = 0.25T + nT, n = 0, 1, 2 \ldots$). It can be found that the results of the HF model are in good agreement with the experimental, indicating that the solution state vector used in the construction of POD-NIROM is reliable. It is worth mentioning that when solving the HF model, the computational domain (2 m × 1 m, equal to the pool used in the experiment) is divided into 23 823 elements and the time step is 1/1000 s. The grid convergence analysis has been performed in figure 3(C), confirming the validity of the results.

3.2. POD analysis

To build the ROM, the snapshot POD analysis is applied to the solution state vector $s(x, t, \theta)$. Specifically, 12 000 snapshots are collected from $s(x, t, \theta)$ (including 60 cases with varied θ), using a time step of $\Delta t = 0.5$ s. The energy $E_\Omega = \lambda_i^{s_i} / \Sigma_i \lambda_i^{s_i}$ associated with the ith POD special mode $\Phi_i^{s_i}$ is shown in figures 4(A) and (B). To ensure that the POD-NIROM comprises 99.8% of the total energy, that is,

$$\frac{\sum_j^{r^{s_i}} \lambda_j^{s_i}}{\sum_i^{n^{s_i}} \lambda_i^{s_i}} \geqslant 99.8\%, \quad (13)$$

$r_\Omega^{s_i} = \left[r_\Omega^{qx}, r_\Omega^{qr}, r_\Omega^{u}, r_\Omega^{v}, r_\Omega^{p} \right] = [15, 16, 264, 278, 81]$ out of $n^{s_i} = 12\,000$ POD special modes are selected (the index of s_i is defined in equation (4)), as shown in figures 4(A) and (B). It can be seen that $r_\Omega^{s_i}$ sets of POD modes are sufficient to capture most of the total energy E_Ω. However, as shown in figures 4(C) and (D), a large number of POD space bases contain fluid features on Γ_{m}. If $r_{\Gamma_{\mathrm{m}}}^{s_i}$ is defined by the principle of equation (13), then thousands of POD special modes will be retained, which makes the computational cost of POD-NIROM unacceptable. Finally, from the perspective of balancing the priority of capturing the total energy and reconstructing the fluid features on Γ_{m}, the $r_{\Gamma_{\mathrm{m}}}^{s_i} = r_\Omega^{s_i} = [15, 16, 264, 278, 81]$ sets of POD basis is selected to reconstruct the boundary features. The predictions of the constructed POD-NIROM are evaluated in subsequent chapters.

Figure 3. The time evolution of the instantaneous hydrodynamic forces acting on the mantle (from $t = 3T$ to $t = 6T$). (A) $k = 0.2$, $T = 2$ s. (B) $k = 0.4$, $T = 2$ s. The red, pink, and yellow dots represent three independent experiments respectively. The black line: HF model simulation, and the blue line: POD-NIROM prediction. (C) $k = 0.5$, $T = 2$ s.

3.3. Construction of LSTM NN-based NIROM

To reproduce the time evolution of the fluid, POD temporal coefficients $a^{s_i}(t)$ are required. Here, LSTM NN is utilized to predict the POD time coefficient. Given the time series of mantle undulations $X_{\mathrm{ma}}(t, \theta_i)$ (under parameter θ_i) as input, LSTM NN tries to construct a nonlinear map that can predict the time evolution of POD temporal coefficients (denoted as $\tilde{a}^{s_i}(t)$, the details are shown in figure 2). The neural network models used in this article are created in the Deep Learning Toolbox developed by MATLAB. In the training of LSTM NN, the adaptive moment estimation [71] is used, which is based on a stochastic gradient descent algorithm [72]. As a standard choice for sequence-to-sequence regression problems, the half-mean-square error (HMSE) of the prediction at each time step is selected as the loss function of the regression layer:

$$\mathrm{HMSE} = \frac{1}{2n_t} \sum_i^{n_t} \sum_j^{r^{s_i}} \left(y_{ij} - \tilde{y}_{ij}\right)^2, \qquad (14)$$
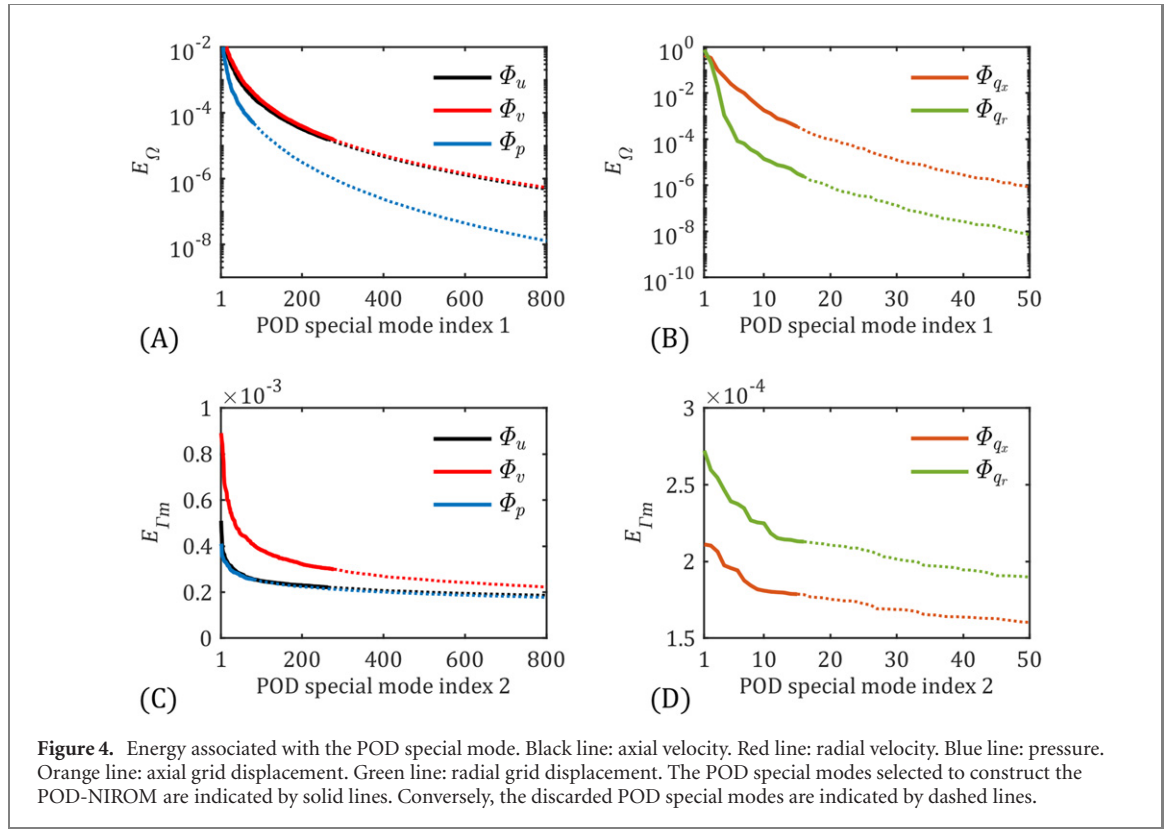
where y_{ij} is the target output, $\tilde{y}_{ij}$ is the network's prediction. For all the training, the learning rate is 0.001 and the batch size is equal to 20. In addition,

20% out of 60 cases are regarded as the test set. Figure 5(A) shows the curves of the validation loss of LSTM NNs varied with epochs, where the performance of NIROM using various numbers of LSTM cells is evaluated. It can be observed that when the number of LSTM units is around 1200, the loss of LSTM NN tends to converge. Note that to avoid overfitting, the training process stops when the maximum epoch is 2000.

4. Results and discussion

4.1. Efficiency of mapping from parameter space to prediction

One of the main purposes of this research is to construct a mapping from the parameter space $\boldsymbol{\theta}(k, T)$ to the solution state vector $\boldsymbol{s}(\boldsymbol{x}, t, \boldsymbol{\theta})$. Based on this mapping, the evolution of the fluid characteristics caused by mantle undulations of the MUPRo can be quickly predicted. Taking from figure 2, the complete prediction process includes pre-processing (converting the specified parameter combination into input) and prediction (predicting the solution state vector and calculating the target function). It is worth mentioning that the prediction includes

Figure 4. Energy associated with the POD special mode. Black line: axial velocity. Red line: radial velocity. Blue line: pressure. Orange line: axial grid displacement. Green line: radial grid displacement. The POD special modes selected to construct the POD-NIROM are indicated by solid lines. Conversely, the discarded POD special modes are indicated by dashed lines.

the evolution of the fluid characteristic for three mantle motion periods (at least 161 time steps are predicted, and the snapshot time step is d$t = 0.05$ s). To evaluate the response time of the proposed model, 4331 predictions with various parameter combinations $(\theta_{ij}(k_i, T_j),\ k_i = 0.1 + 0.01i, T_j = 1.5 + 0.025j,\ i = 0, 1, \ldots, 70, j = 0, 1, \ldots, 60)$ have been performed, and the time-consuming of the complete prediction has been monitored (as shown in figures 5(B) and (C)).

The mean calculation cost of preprocessing is 0.2 s, and the mean response time for each prediction is 0.34 s. Therefore, the average computational cost of one prediction (with 200 snapshots) using the trained POD-NIROM is 0.54 s. Compared with the model that extracts the input from the solution state vector of the full-order HF model, the proposed model can update the input more efficiently, considering that the input of the proposed model is collected from the mantle dynamics governed by the sine function (equation (10)). For reference, it takes around 950 s to extract all 200 snapshots of a case using the full-order HF model proposed in this article (equations (2) and (3)), the computational cost of the proposed POD-NIROM training process is 304 s and it takes 2340 s to predict the above 4331 cases using the trained POD-NIROM.

In summary, consistent with most existing ROMs, the prediction process of the proposed POD-NIROM is completely independent of the full-order HF model, and has higher computational efficiency than the HF model when predicting a single case. Moreover, the

preprocessing stage of the proposed model is also completely independent of the full-order HF model. For the prediction of new cases that need to update the input, the input of the proposed POD-NIROM is extracted from the mantle kinematics (driven by the classical sine equation), which makes the preprocessing more efficient. In contrast, the input of some existing ROMs [20, 48, 49] is still extracted from the full-order HF model, and these models may not be suitable for predicting new cases that require the updated input.

4.2. Reliability of prediction using the proposed POD-NIROM

Another goal of the proposed methodology is to quickly and reliably predict the evolution of the flow field caused by different mantle undulations of the MUPRo. Figure 6 shows the comparison between the predictions $\tilde{a}^{s_i}$ (based on LSTM NN) and expectations a^{s_i} (calculated by equation (6)) of the POD temporal coefficients in four cases of various parameter combinations. LSTM NN is capable of predicting the POD temporal coefficients $\tilde{a}^{s_i}$, taking $x(t, \boldsymbol{\theta})$, the normalization of MUPRo's mantle motion $\boldsymbol{X}_{\text{ma}}(t, \boldsymbol{\theta})$, as input.

The predicted POD temporal coefficients $\tilde{a}^{s_i}$ are used to reconstruct the flow field characteristics (represented by the solution state vector s_i), according to equation (6). The time evolution of flow field characteristics is the basis for optimizing the mantle propulsion parameters of MUPRo.
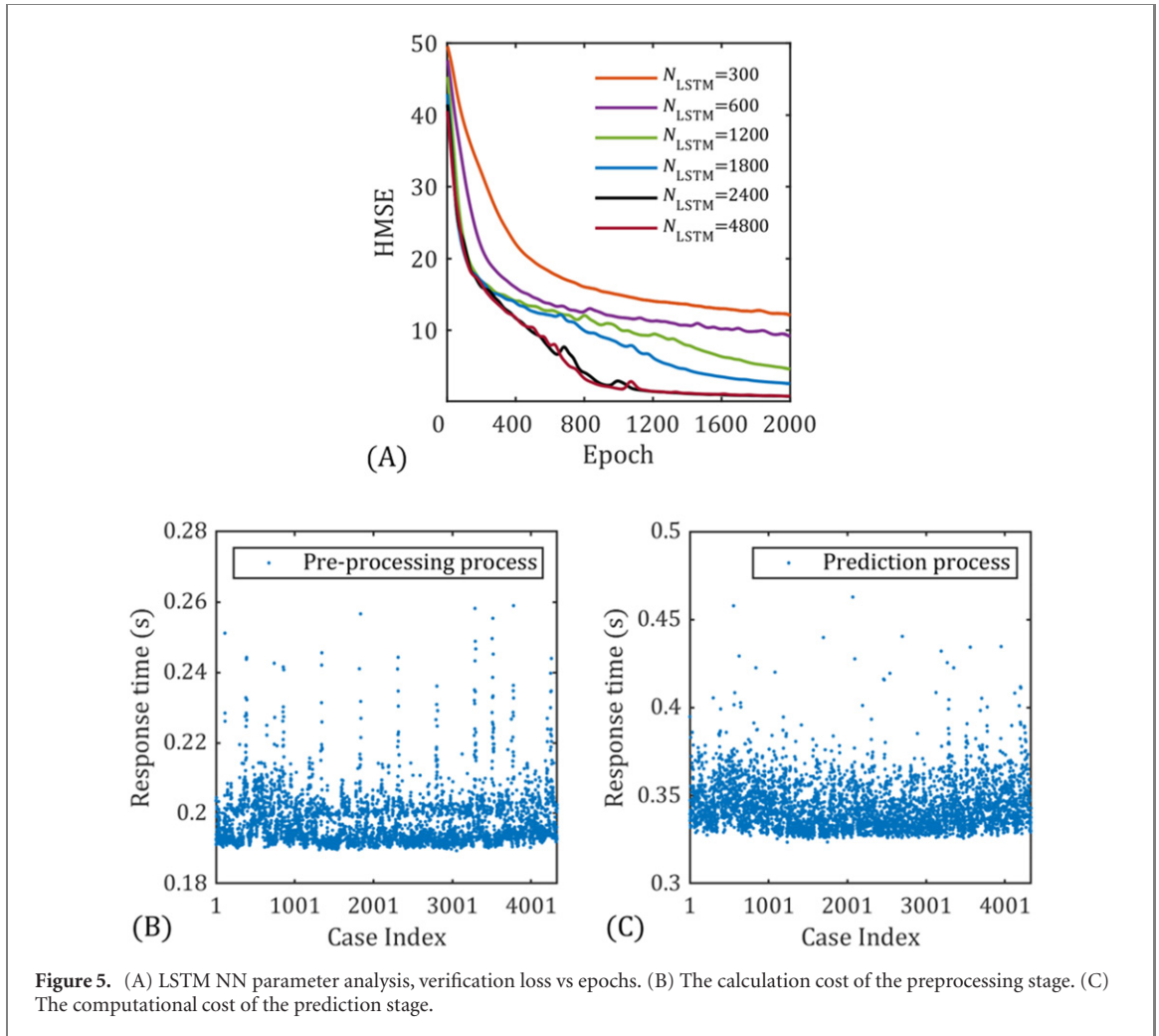
Figure 5. (A) LSTM NN parameter analysis, verification loss vs epochs. (B) The calculation cost of the preprocessing stage. (C) The computational cost of the prediction stage.

To evaluate the prediction of the proposed POD-NIROM (whose prediction is represented by s_{prd2}), the NIROM combined with the classic POD method (where only $r_{\Omega}^{s_i}$ POD base is retained and the prediction is represented by s_{prd1}) is also constructed and used as a reference. To intuitively evaluate the reliability of the prediction of flow characteristics, some snapshots of the fully developed flow field are shown in figure 7. The four subgraphs in figure 7 correspond to the four working conditions in figure 6 respectively.

The fluid characteristics in Ω predicted by the proposed POD-NIROM are consistent with the classic POD method predictions (shown in figure 7). The total energy additionally captured by the proposed model is defined as follows:

$$\Delta E_{\Omega}^{s_i} = \frac{\sum_{i=1}^{r_{\Gamma_m}^{s_i}} \lambda_i^{s_i}}{\sum_{i=1}^{n^{s_i}} \lambda_i^{s_i}}. \tag{15}$$

After calculations, $\Delta E_{\Omega}^{s_i} = \left[\Delta E_{\Omega}^{q_x}, \Delta E_{\Omega}^{q_r}, \Delta E_{\Omega}^{u}, \Delta E_{\Omega}^{v}, \Delta E_{\Omega}^{p}\right] = [1.2 \times 10^{-17}, 4.1 \times 10^{-18}, 1.6 \times 10^{-15}, 2.7 \times 10^{-15}, 8.3 \times 10^{-17}]$. The result is consistent with the explanation in the previous chapter, that is, the contribution of the additional boundary-feature-favored POD modes to the total energy capture is almost zero. Figure 8 shows the fluid properties on

Γ_{m} predicted by the proposed model. To facilitate comparison, comparisons of the mean relative errors (represented by the dotted line in figure 8) between the proposed POD-NIROM and NIRON with the classical POD method are shown in table 1. Intuitively, the proposed POD-NIROM has a lower order relative error when predicting the velocity on the boundary. Furthermore, the mean relative error of pressure predictions is higher compared to velocity predictions. This phenomenon may be caused by the existence of points on the boundary where p_{HF} (considered as the true value) is equal to zero. However, from the comparison of predictions when $p_{\mathrm{HF}} \neq 0$, a lower order δ_p can be found when using the proposed POD-NIROM for boundary pressure predictions.

In conclusion, the proposed POD-NIROM can more reliably predict the fluid characteristics on the boundary which is used to calculate the instantaneous hydrodynamic force acting on the MUPRo.

4.3. Analysis and optimization of mantle motion parameters

Using the prediction of the proposed POD-NIROM, the mantle motion parameters are evaluated to optimize the propulsion effect. The evaluated mantle
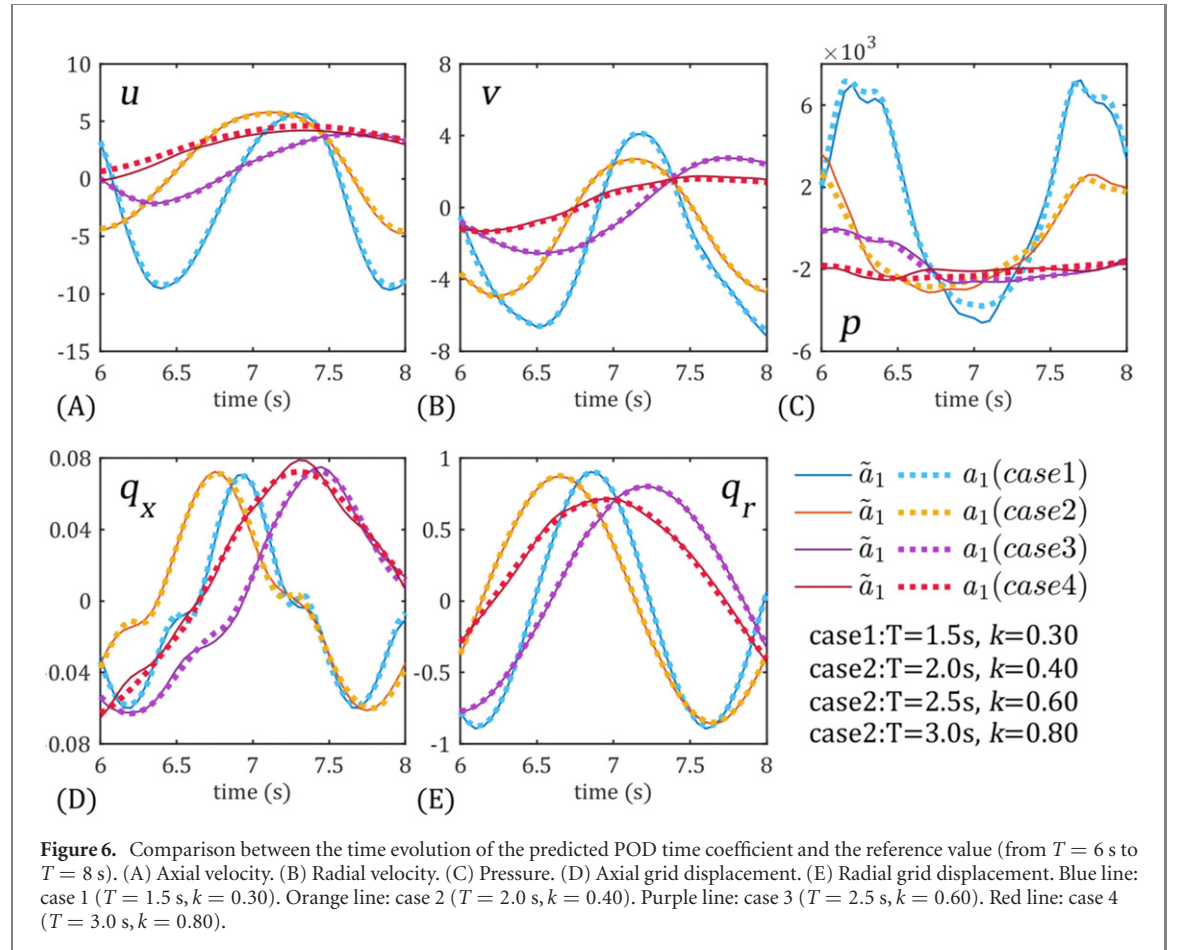
Figure 6. Comparison between the time evolution of the predicted POD time coefficient and the reference value (from $T = 6$ s to $T = 8$ s). (A) Axial velocity. (B) Radial velocity. (C) Pressure. (D) Axial grid displacement. (E) Radial grid displacement. Blue line: case 1 ($T = 1.5$ s, $k = 0.30$). Orange line: case 2 ($T = 2.0$ s, $k = 0.40$). Purple line: case 3 ($T = 2.5$ s, $k = 0.60$). Red line: case 4 ($T = 3.0$ s, $k = 0.80$).

Table 1. Comparison of the mean relative error $\overline{\delta}$ between the proposed POD-NIROM and the NIROM with the classic POD method.

	Case 1		Case 2		Case 3		Case 4	
	$\overline{\delta}u_{\mathrm{prd}}$	$\overline{\delta}p_{\mathrm{prd}}$	$\overline{\delta}u_{\mathrm{prd}}$	$\overline{\delta}p_{\mathrm{prd}}$	$\overline{\delta}u_{\mathrm{prd}}$	$\overline{\delta}p_{\mathrm{prd}}$	$\overline{\delta}u_{\mathrm{prd}}$	$\overline{\delta}p_{\mathrm{prd}}$
Proposed POD-NIROM	0.027	0.094	0.020	0.112	0.020	0.111	0.084	0.058
NIROM with classic POD	1.016	0.727	0.972	0.318	0.925	0.326	1.333	0.886

motion parameters include undulation period T and body wave number k. The optimization index is the time average value of the hydrodynamic forces acting on the mantle $\langle F \rangle$ in three swimming cycles (from $t = 3T$ to $t = 6T$). $\langle F \rangle$ can be calculated as follows:

$$\langle F \rangle = \frac{1}{3T} \int_{3T}^{6T} \left[\int_{\Gamma_m} \left(-pn_x + \tau_{xx}n_x + \tau_{xr}n_r \right) \mathrm{d}\Gamma_m \right] \mathrm{d}t. \quad (16)$$
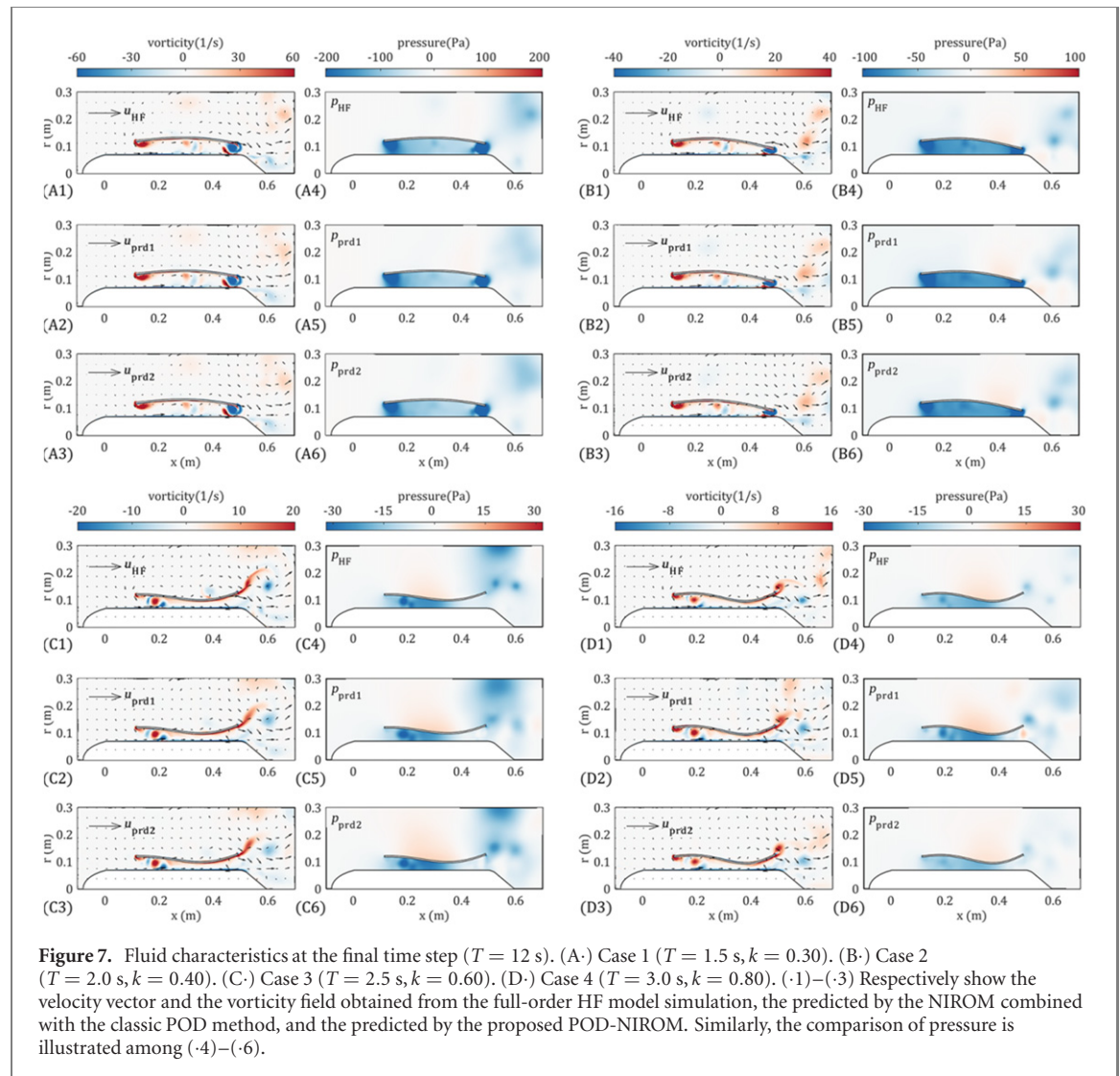
Concurrently, the cost of MUPRo startup (represented by the time average of the total power $\langle P \rangle$) is also considered. $\langle P \rangle$ includes the propulsion power $\langle P_x \rangle$ and the lateral power loss $\langle P_r \rangle$ (equation (17)). The calculation of $\langle P_r \rangle$ is defined in equation (19) [66] and the definition of $\langle P_x \rangle$ is similar to $\langle P_r \rangle$ (equation (18))

$$\langle P \rangle = \langle P_x \rangle + \langle P_r \rangle, \quad (17)$$

$$\langle P_x \rangle = \frac{1}{3T} \int_{3T}^{6T} \left[\int_{\Gamma_m} \left(-pn_x + \tau_{xx}n_x + \tau_{xr}n_r \right) \dot{X}_{\mathrm{ma}} \, \mathrm{d}\Gamma_m \right] \mathrm{d}t, \quad (18)$$

$$\langle P_r \rangle = \frac{1}{3T} \int_{3T}^{6T} \left[\int_{\Gamma_m} \left(-pn_r + \tau_{rx}n_x + \tau_{rr}n_r \right) \dot{R}_{\mathrm{ma}} \, \mathrm{d}\Gamma_m \right] \mathrm{d}t, \quad (19)$$

where the velocity of mantle $\dot{X}_{\mathrm{ma}} = \left[\dot{X}_i(t), \dot{R}_i(t) \right]$ is defined in section 2.2. In addition, there is another method to calculate the power required for the robot transport from the perspective of fluid energy conservation, which mainly focuses on the wake behind the swimmer [73]. However, conclusions based on wake vortices can be misleading [74], and the startup cost of MUPRo is not discussed in terms of fluid energy conservation.

Figure 7. Fluid characteristics at the final time step ($T = 12$ s). (A·) Case 1 ($T = 1.5$ s, $k = 0.30$). (B·) Case 2 ($T = 2.0$ s, $k = 0.40$). (C·) Case 3 ($T = 2.5$ s, $k = 0.60$). (D·) Case 4 ($T = 3.0$ s, $k = 0.80$). (·1)–(·3) Respectively show the velocity vector and the vorticity field obtained from the full-order HF model simulation, the predicted by the NIROM combined with the classic POD method, and the predicted by the proposed POD-NIROM. Similarly, the comparison of pressure is illustrated among (·4)–(·6).

The two parameters (k and T) are critical for the propulsion performance of the undulating mantle. Under a constant undulation period ($T = 2$ s), the variation of the mean propulsion force $\langle F \rangle$ for all experiments, simulations, and predictions is shown in figure 9(A). It is easy to find out that for the mantle motion under $T = 2$ s, the prediction of $\langle F \rangle$ has a local optimum $\langle F_{\text{prd}} \rangle_{\text{max}} = 2.014$ N m^{-1} (when $k = 0.3$). Moreover, similar trends are also presented in simulations and experiments. The experiments, simulations, and predictions, shown in figure 9(B), illustrate that for a constant body wave number ($k = 0.5$), $\langle F \rangle$ increases as the undulation period T decreases.

Figure 9(C) shows the $\langle F_{\text{prd}} \rangle$ predicted by proposed POD-NIROM under all parameter combinations θ_i. For the optimal combination of k and T, $\langle F_{\text{prd}} \rangle_{\text{max}}$ is located at the ridgeline, indicated by the green line in figure 9(C). By observing the ridgeline, it is obvious that for any $T \in [1.5 \text{ s}, 3 \text{ s}]$ ($\langle F_{\text{prd}} \rangle$ when $T = 2$ s or $T = 2.5$ s is shown in figures 10(B) and (C), respectively), $\langle F_{\text{prd}} \rangle$ exhibits a local maximum around $k = 0.3$.

One of the main goals of this paper is to find the combination of mantle propulsion parameters when

the propulsion force (for the MUPRo startup) is optimal, which is discussed above. But generally, greater propulsion is often accompanied by the high cost of the MUPRo startup. Therefore, another goal of this article is to find the best combination of parameters that control the mantle motion, when the cost of the MUPRo startup is constant. Based on equation (19), the cost of MUPRo startup $\langle P_{\text{prd}} \rangle$ under various combinations of parameters is predicted and illustrated in figure 9(D).

The definition of a swimmer's efficiency is still controversial. In recent years, Froude efficiency has been frequently used in research [66, 75, 76]. However, Froude efficiency is only meaningful when swimming forward at a constant speed U_∞ and $\langle F \rangle = 0$. Therefore, it does not apply to the scenario of MUPRo startup, that is, $U_\infty = 0$, $\langle F \rangle \neq 0$. As an alternative method to find the parameter combination with the best propulsion efficiency, the startup thrust received by MUPRo under different parameter combinations is discussed when the cost of MUPRo startup $\langle P_{\text{prd}} \rangle$ is constant. For the convenience of comparison, $\langle F_{\text{prd}} \rangle$ and $\langle P_{\text{prd}} \rangle$ with various parameter combinations are plotted in the same figure
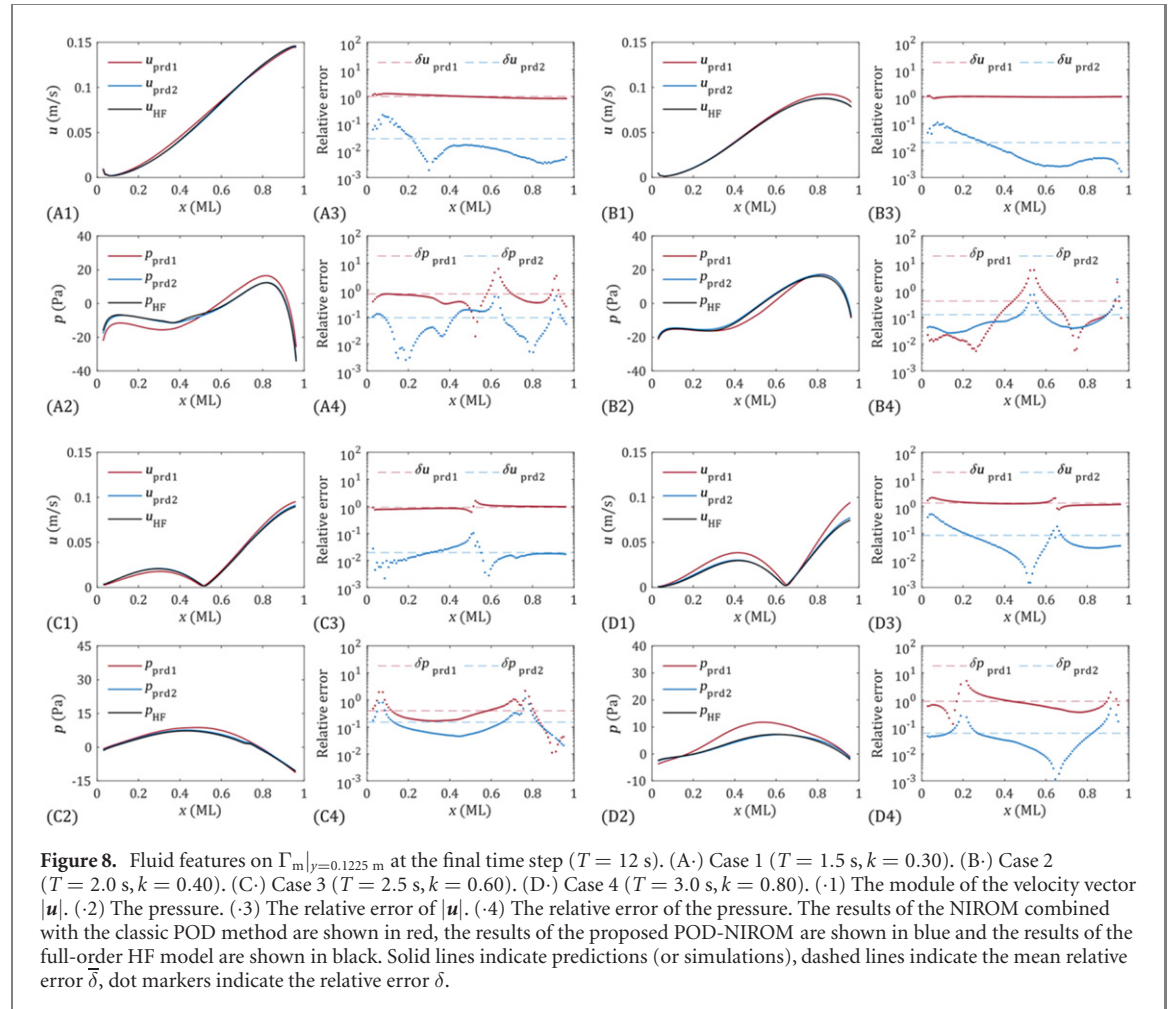
Figure 8. Fluid features on $\Gamma_{\rm m}|_{y=0.1225\,{\rm m}}$ at the final time step ($T = 12$ s). (A·) Case 1 ($T = 1.5$ s, $k = 0.30$). (B·) Case 2 ($T = 2.0$ s, $k = 0.40$). (C·) Case 3 ($T = 2.5$ s, $k = 0.60$). (D·) Case 4 ($T = 3.0$ s, $k = 0.80$). (·1) The module of the velocity vector $|\boldsymbol{u}|$. (·2) The pressure. (·3) The relative error of $|\boldsymbol{u}|$. (·4) The relative error of the pressure. The results of the NIROM combined with the classic POD method are shown in red, the results of the proposed POD-NIROM are shown in blue and the results of the full-order HF model are shown in black. Solid lines indicate predictions (or simulations), dashed lines indicate the mean relative error $\overline{\delta}$, dot markers indicate the relative error δ.

(figure 10(A)), represented by two different colors. Figures 10(B) and (C) are respectively taken from the two black dashed lines in figure 10(A). These two figures more intuitively show that accelerating the frequency of mantle motion can increase propulsion, but also increase the cost $\langle P_{\rm prd} \rangle$. At the same time, increasing the body wave number can effectively reduce the cost $\langle P_{\rm prd} \rangle$.

Figures 10(D)–(F) are drawn along the three contours of the cost of MUPRo startup $\langle P_{\rm prd} \rangle$ in figure 10(A) (indicated by blue lines) and describe $\langle F_{\rm prd} \rangle$ (indicated by orange lines) when $\langle P_{\rm prd} \rangle =$ 0.4 W m^{-1}, 0.6 W m^{-1}, and 0.8 W m^{-1}, respectively. The corresponding parameter combinations are indicated by green lines. For a given cost $\langle P_{\rm prd} \rangle$, a larger starting thrust ($\langle F_{\rm prd} \rangle$, orange line) occurs when a large k and small T (along the green line) are chosen as parameters.

In summary, in the parameter combination considered in this study ($A_{\rm m} = 0.1ML$, as a common value for fish kinematics), the peak of $\langle F_{\rm prd} \rangle$ appears near $k = 0.3$. When the power loss is constant, the undulation of the mantle with a large k is more likely to bring greater startup propulsion $\langle F_{\rm prd} \rangle$ to MUPRo. For the mantle to undulate with a smaller wave number ($k < 0.5$), its motion should be more

like a swing (rather than a wave), which can produce greater propulsion, but the cost $\langle P_{\rm prd} \rangle$ cannot be underestimated.

4.4. Estimation of the MUPRo startup performance

The starting direction of fish from rest is often inconsistent with the axis direction because of its asymmetrical motion [77]. In contrast, the jellyfish-inspired MUPRo has better orientation at startup because of its rotationally symmetric undulating motion [50–52].

From observation, the undulation of the MUPRo is similar to fish locomotion. The flow characteristics (especially in figure 7(D)) downstream of the MUPRo can be summarized, that is, the vortex rotates counterclockwise (positive vorticity, represented by the red area) when $|r| > 120$ mm, and when $|r| < 120$ mm, the vortex rotates clockwise (negative vorticity, represented by the blue area). The wakes described above can be regarded as a reverse Karman vortex street, which is a jet that generates thrust on the MUPRo [78].

The instantaneous thrust of the MUPRo has a consistent trend with other jellyfish-inspired robots (as described in section 3.1) [5]. Considering that the startup thrust is directly affected by the size of the swimmer, in this section, the time-averaged startup
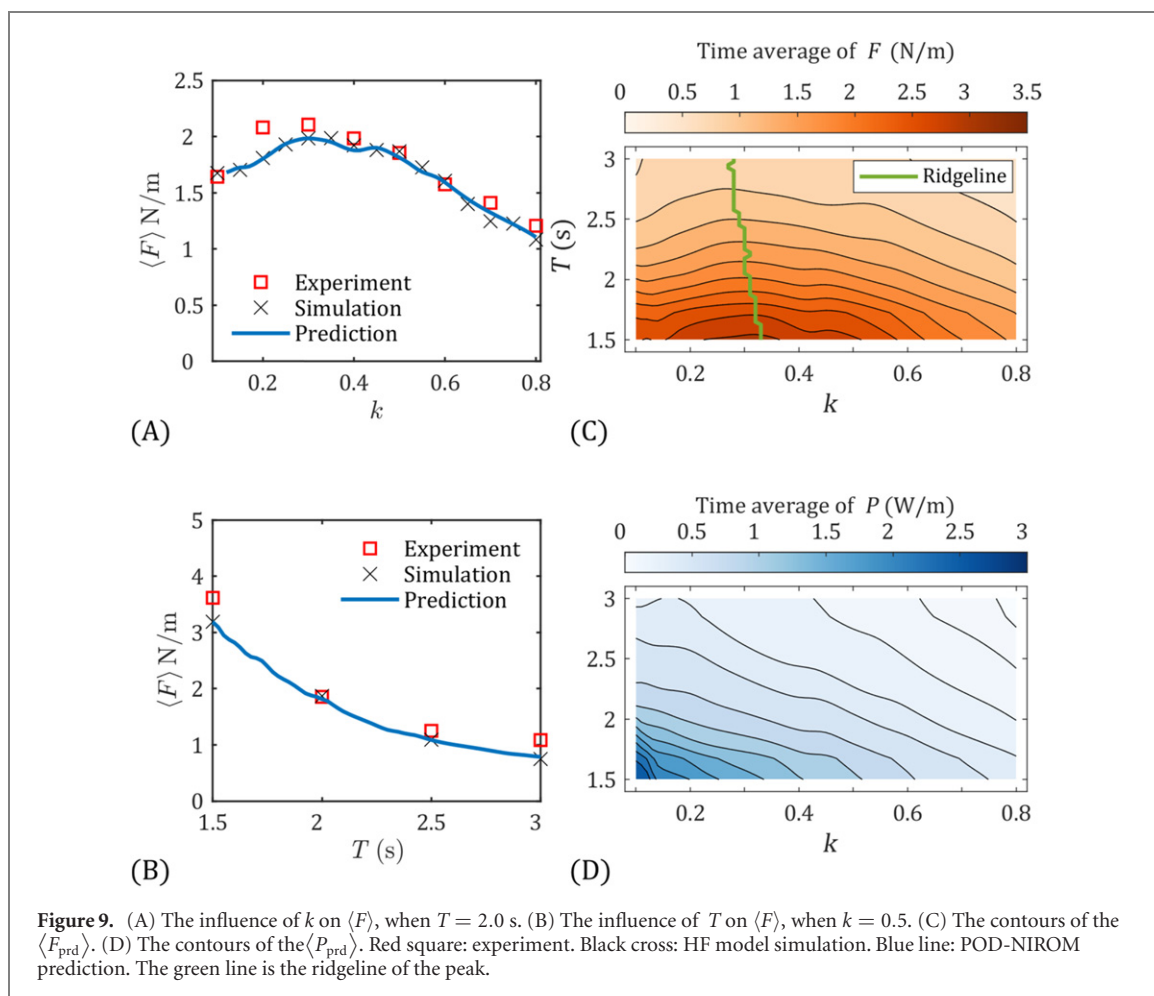
Figure 9. (A) The influence of k on $\langle F \rangle$, when $T = 2.0$ s. (B) The influence of T on $\langle F \rangle$, when $k = 0.5$. (C) The contours of the $\langle F_{prd} \rangle$. (D) The contours of the $\langle P_{prd} \rangle$. Red square: experiment. Black cross: HF model simulation. Blue line: POD-NIROM prediction. The green line is the ridgeline of the peak.

Table 2. Comparison between startup acceleration of the MUPRo and peak acceleration of two species [6, 67, 79].

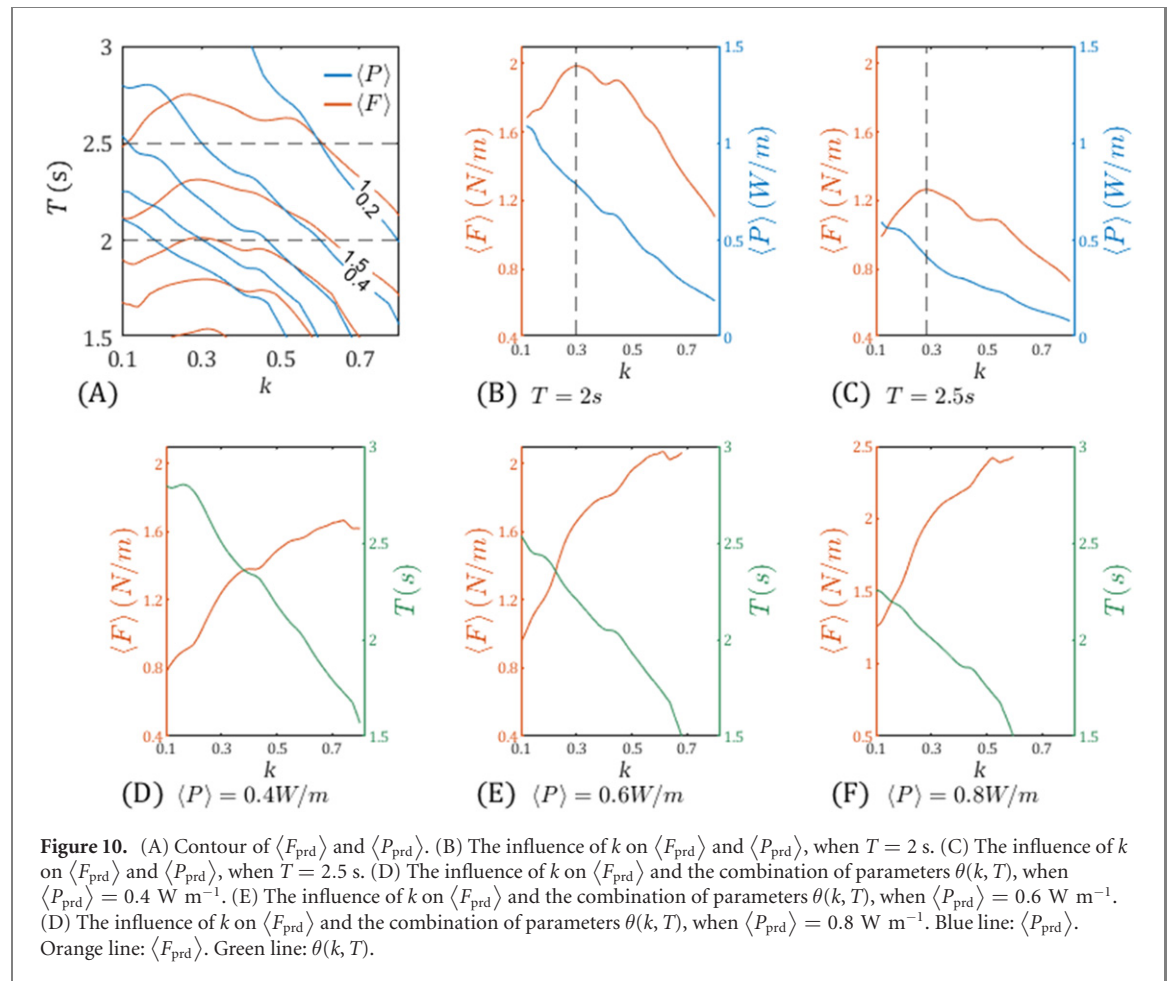|	MUPRo			*Aequorea victoria*	*Phialidium gregarium*
Fineness ratio		0.357		[0.42, 0.55]	[0.5, 0.7]
Acceleration (mm s^{-2})	28.5	44.8	77.3	50	100
Frequency (Hz)	0.4	0.5	0.67	1.1	1.67
Wave number	0.26	0.28	0.33		
Maximum lateral deformation	10%	10%	10%	30%	46%

acceleration $\langle a_s \rangle$ is used to evaluate the startup performance of the MUPRo. $\langle a_s \rangle$ is defined as follows,

$$\langle a_s \rangle = \frac{\langle F \rangle}{\rho_s S}, \tag{20}$$

where ρ_s is the average density of the MUPRo ($\rho_s \approx 1000$ kg m^{-3}, considering that the MUPRo is generally suspended in water), $S = 0.0443$ m^2 is the area of the longitudinal section (figure 1(B)). It is worth mentioning that $\langle F \rangle$ is a 2D force (of which the unit is N m^{-1}). Table 1 shows the comparison between the startup acceleration of the MUPRo and the peak acceleration of four different species [6, 67, 79]. The time-averaged startup acceleration $\langle a_s \rangle$ of the MUPRo at $T = 1.5$ s, $T = 2$ s (the case indicated by the dotted line in figure 10(B)) and $T = 2.5$ s (the case indicated by the dotted line in figure 10(C)) are shown in table 2. It can be found

that when the MUPRo undulates at a frequency of 0.5 Hz, the time-averaged startup acceleration of the MUPRo is close to the peak acceleration of *Aequorea victoria* moving at a frequency of 1.1 Hz. When generating an acceleration of about 45 mm s^{-2}, the MUPRo requires smaller cross-sectional deformation and slower frequency than *Aequorea victoria*, which means the MUPRo has a smaller transportation cost.

For simplicity, a 2D assumption made judging from the domain dimensions is applied in this paper to simulate and predict the startup performance of the MUPRo. The current discussion on the MUPRo's startup performance guides the design of the MUPRo's 3D prototype. Compared with the experiments in this paper, the current predictions additionally apply the axisymmetric assumption, and the predictions may be inaccurate. The 2D computational domain applied in the current work can be

Figure 10. (A) Contour of $\langle F_{\mathrm{prd}} \rangle$ and $\langle P_{\mathrm{prd}} \rangle$. (B) The influence of k on $\langle F_{\mathrm{prd}} \rangle$ and $\langle P_{\mathrm{prd}} \rangle$, when $T = 2$ s. (C) The influence of k on $\langle F_{\mathrm{prd}} \rangle$ and $\langle P_{\mathrm{prd}} \rangle$, when $T = 2.5$ s. (D) The influence of k on $\langle F_{\mathrm{prd}} \rangle$ and the combination of parameters $\theta(k, T)$, when $\langle P_{\mathrm{prd}} \rangle = 0.4$ W m^{-1}. (E) The influence of k on $\langle F_{\mathrm{prd}} \rangle$ and the combination of parameters $\theta(k, T)$, when $\langle P_{\mathrm{prd}} \rangle = 0.6$ W m^{-1}. (D) The influence of k on $\langle F_{\mathrm{prd}} \rangle$ and the combination of parameters $\theta(k, T)$, when $\langle P_{\mathrm{prd}} \rangle = 0.8$ W m^{-1}. Blue line: $\langle P_{\mathrm{prd}} \rangle$. Orange line: $\langle F_{\mathrm{prd}} \rangle$. Green line: $\theta(k, T)$.

mapped to 3D (according to the principle of rotational symmetry). However, compared with the 3D prototype, the mapping solution is different because connections between the mantle and the main cabin (shown in figure 1(A)) are ignored in the mapping solution.

5. Conclusion

In this article, an underwater robot inspired by jellyfish (MUPRo) has been designed, and is propelled by mantle motion. The proposed POD-NIROM, which has attractive computational efficiency and reliable predictions (especially fluid characteristics on the boundary) when predicting new models, is proposed to find the optimal combination of parameters that control mantle undulations. The proposed model makes full use of POD and LSTM NN to quickly and effectively predict the evolution of flow field characteristics around the MUPRo caused by mantle movement.

Compared with the classic POD methods, the proposed model can more reliably predict the evolution of fluid characteristics on the specified boundaries. Moreover, as a simplified alternative to extracting input from the full-order HF model, the input of the proposed POD-NIROM is extracted from the mantle

kinematics (controlled by the classical sine equation), which allows the proposed model to update the input more efficiently. The low computational cost of the preprocessing stage means that the proposed POD-NIROM also has attractive computational efficiency when predicting new cases. The computational cost of a simulation using the current HF model is about 800 s. However, within 800 s, the proposed POD-NIROM can perform more than 1400 predictions.

The proposed POD-NIROM establishes a direct relationship between the boundary motion of the flow field (caused by the mantle motion) and the time evolution of the flow field characteristics. At the same time, the proposed model can update the input faster, which means it is more suitable for optimization that needs to consider a large number of new cases.

The reliability of the proposed POD-NIROM has been discussed, where predictions were compared with experiments. The solution state vector (describes the evolution of the flow field characteristics) under various parameter combinations was predicted to analyze the optimal combination of parameters controlling mantle motion. The main findings of this work are summarized as follows.

Through experiments and predictions in this paper, it has been seen that in a single mantle motion cycle, the mantle provides two propulsion strokes for

the MUPRo (the peak values of the two strokes are different, due to the design of the MUPRo). This finding is consistent with fish movement, indicating that it is feasible to use fish kinematics to guide the MUPRo's mantle motion.

For a constant period of mantle undulation $T \in [1.5\,\text{s}, 3\,\text{s}]$, when the mantle motion is characterized by $k = 0.3$ (the mantle motion is more like swinging), $\langle F_{\text{prd}} \rangle$ is greater, and $\langle P_r^{\text{prd}} \rangle$ is also very considerable. When k is around 0.3, $\langle F_{\text{prd}} \rangle$ reaches the local maximum. Among the parameter combinations discussed in this article, for a constant $\langle P_r^{\text{prd}} \rangle$, when $k > 0.5$ (that is, the mantle motion is more like a wave), $\langle F_{\text{prd}} \rangle$ acting on the MUPRo is greater.

Compared with *Aequorea victoria*, the proposed MUPRo requires lower frequency and smaller amplitude when generating a startup acceleration of 45 mm s^{-2}, which means that the proposed MUPRo has a good startup performance.

Consequently, this research provides a new method for the optimization of propulsion parameters of jellyfish-inspired robots, and theoretically supports the selection of MUPRo driving parameters. In the future, the method proposed in this paper can be developed further and applied to the research on forwarding swimming or turning actions of biomimetic robots. Future work includes developing a self-propelled 3D prototype of the MUPRo and analyzing the performance of the MUPRo from the perspective of transportation cost and swimming gait control.

Acknowledgments

Data availability statement

The data that support the findings of this study are available upon reasonable request from the authors.

ORCID iDs

Zixiang Ying ⓘ https://orcid.org/0000-0003-0637-9819

References

[1] Omori M and Kitamura M 2004 Taxonomic review of three Japanese species of edible jellyfish (Scyphozoa: Rhizostomeae) *Plankton Biol. Ecol.* **51** 36–51

[2] Colin S P and Costello J H 2002 Morphology, swimming performance and propulsive mode of six co-occurring hydromedusae *J. Exp. Biol.* **205** 427–37

[3] Sahin M, Mohseni K and Colin S P 2009 The numerical comparison of flow patterns and propulsive performances for the hydromedusae Sarsia tubulosa and Aequorea victoria *J. Exp. Biol.* **212** 2656–67

[4] Dabiri J O, Colin S P, Costello J H and Gharib M 2005 Flow patterns generated by oblate medusan jellyfish: field measurements and laboratory analyses *J. Exp. Biol.* **208** 1257–65

[5] Frame J, Lopez N, Curet O and Engeberg E D 2018 Thrust force characterization of free-swimming soft robotic jellyfish *Bioinspiration Biomimetics* **13** 064001

[6] Najem J *et al* 2012 Biomimetic jellyfish-inspired underwater vehicle actuated by ionic polymer metal composite actuators *Smart Mater. Struct.* **21** 094026

[7] Marut K, Stewart C, Michael T, Villanueva A and Priya S 2013 A jellyfish-inspired jet propulsion robot actuated by an iris mechanism *Smart Mater. Struct.* **22** 094021

[8] Renda F *et al* 2015 Modelling cephalopod-inspired pulsed-jet locomotion for underwater soft robots *Bioinspiration Biomimetics* **10** 055005

[9] Hu J, Li H and Chen W 2021 A squid-inspired swimming robot using folding of origami *J. Eng.* **2021** 630–9

[10] Villanueva A, Smith C and Priya S 2011 A biomimetic robotic jellyfish (Robojelly) actuated by shape memory alloy composite actuators *Bioinspiration Biomimetics* **6** 036004

[11] Dabiri J O, Colin S P, Katija K and Costello J H 2010 A wake-based correlate of swimming performance and foraging behavior in seven co-occurring jellyfish species *J. Exp. Biol.* **213** 1217–25

[12] Videler J J and Hess F 1984 Fast continuous swimming of two pelagic predators, saithe (Pollachius virens) and mackerel (Scomber scombrus): a kinematic analysis *J. Exp. Biol.* **109** 209

[13] Nelson J S, Grande T C and Wilson M V H 2016 *Fishes of the World* 5th edn (New York: Wiley) https://doi.org/10.1002/9781119174844

[14] Dabiri J O, Colin S P and Costello J H 2006 Fast-swimming hydromedusae exploit velar kinematics to form an optimal vortex wake *J. Exp. Biol.* **209** 2025–33

[15] Triantafyllou M S, Triantafyllou G S and Yue D K P 2000 Hydrodynamics of fishlike swimming *Annu. Rev. Fluid Mech.* **32** 33–53

[16] Triantafyllou M S and Triantafyllou G S 1995 An Efficient Swimming Machine *Scientific American* **272** 64–70

[17] Lauder G V and Tytell E D 2005 Hydrodynamics of undulatory propulsion *Fish Physiol.* **23** 425–68

[18] Marchese A D, Onal C D and Rus D 2014 Autonomous soft robotic fish capable of escape maneuvers using fluidic elastomer actuators *Soft Robot.* **1** 75–87

[19] Alamir M *et al* 2007 Feedback design for 3D movement of an Eel-like robot *Robotics and Automation, 2007 IEEE Int. Conf.* (Rome, Italy 10–14 April 2007) pp 256–61

[20] Kherad M, Moayyedi M K and Fotouhi F 2020 Reduced order framework for convection dominant and pure diffusive problems based on combination of deep LSTM and POD/DMD methods *Int. J. Numer. Methods Fluids* **93** 853–73

[21] Lozovskiy A, Farthing M, Kees C and Gildin E 2016 POD-based model reduction for stabilized finite element approximations of shallow water flows *J. Comput. Appl. Math.* **302** 50–70

[22] Răzvan Ș, Sandu A and Navon I M 2014 Comparison of POD reduced order strategies for the nonlinear 2D shallow water equations *Int. J. Numer. Methods Fluids* **76** 497–521

[23] Rowley C W, Mezić I, Bagheri S, Schlatter P and Henningson D S 2009 Spectral analysis of nonlinear flows *J. Fluid Mech.* **641** 115

[24] Schmid P J, Li L, Juniper M P and Pust O 2010 Applications of the dynamic mode decomposition *Theor. Comput. Fluid Dyn.* **25** 249–59

[25] Bistrian D A and Navon I M 2017 The method of dynamic mode decomposition in shallow water and a swirling flow problem *Int. J. Numer. Methods Fluids* **83** 73–89

[26] Alekseev A *et al* 2016 On linear and nonlinear aspects of dynamic mode decomposition *Int. J. Numer. Methods Fluids* **82** 348–71

[27] Tu J *et al* 2013 On dynamic mode decomposition: theory and applications *J. Comput. Dyn.* **1** 391–421

[28] Lumley J 1967 The structure of inhomogeneous turbulence *Atmos. Turbul. Radio Wave Propag.* 166–78

[29] Dragomirescu I, Resiga R and Muntean S 2013 Proper orthogonal decomposition method in swirling flows applications *AIP Conf. Proc.* **1558** 1349–52

[30] Perrin R *et al* 2006 3D circular cylinder *Notes on Numerical Fluid Mechanics* **4** 299–312

[31] Zhao X, Wu C, Chen Z, Yang L and Shu C 2020 Reduced order modeling-based discrete unified gas kinetic scheme for rarefied gas flows *Phys. Fluids* **32** 067108

[32] Videler J, Müller U and Stamhuis E J 2000 Aquatic vertebrate locomotion: wakes from body waves *J. Exp. Biol.* **202** 3423–30

[33] Zhao Y *et al* 2019 A modified proper orthogonal decomposition method for flow dynamic analysis *Comput. Fluids* **182** 28–36

[34] Erwan L and Hamdouni A 2010 Reduced order modelling method via proper orthogonal decomposition (POD) for flow around an oscillating cylinder *J. Fluid Struct.* **26** 292–311

[35] Erwan L, Benaouicha M and Hamdouni A 2007 Proper orthogonal decomposition investigation in fluid structure interaction *Eur. J. Comput. Mech.* **16** 401–18

[36] Burkardt J, Gunzburger M and Lee H-C 2006 POD and CVT-based reduced-order modeling of Navier–Stokes flows *Comput. Methods Appl. Mech. Eng.* **196** 337–55

[37] Rapun M-L and Vega J 2010 Reduced order models based on local POD plus Galerkin projection *J. Comput. Phys.* **229** 3046–63

[38] Carlberg K, Bou-Mosleh C and Farhat C 2011 Efficient non-linear model reduction via a least-squares Petrov–Galerkin projection and compressive tensor approximations *Int. J. Numer. Methods Eng.* **86** 155–81

[39] Imran A, Nayfeh A and Ribbens C 2009 On the stability and extension of reduced-order Galerkin models in incompressible flows. A numerical study of vortex shedding *Theor. Comput. Fluid Dyn.* **23** 213–37

[40] Rempfer D 2000 On low-dimensional Galerkin models for fluid flow *Theor. Comput. Fluid Dyn.* **14** 75–88

[41] Halder R, Damodaran M and Khoo B 2020 Deep learning based reduced order model for airfoil-Gust and aeroelastic interaction *AIAA J.* **58** 1–18

[42] Kutz J N 2017 Deep learning in fluid dynamics *J. Fluid Mech.* **814** 1–4

[43] Brunton S, Noack B and Koumoutsakos P 2020 Machine learning for fluid mechanics *Annu. Rev. Fluid Mech.* **52** 477–508

[44] Videler J J and Wardle C S 1991 Fish swimming stride by stride: speed limits and endurance *Rev. Fish Biol. Fisheries* **1** 23–40

[45] LeCun Y, Bengio Y and Hinton G 2015 Deep learning *Nature* **521** 436–44

[46] Baldi P and Hornik K 1989 Neural networks and principal component analysis: learning from examples without local minima *Neural Netw.* **2** 53–8

[47] Bourlard H and Kamp Y 1988 Auto-association by multilayer perceptrons and singular value decomposition *Biol. Cybern.* **59** 291–4

[48] Mohan A and Gaitonde D 2018 A deep learning based approach to reduced order modeling for turbulent flow control using LSTM neural networks (arXiv:1804.09269)

[49] Wang Z *et al* 2017 Model identification of reduced order fluid dynamics systems using deep learning *Int. J. Numer. Methods Fluids* **86** 255–68

[50] Roper D T, Sharma S, Sutton R and Culverhouse P 2011 A review of developments towards biologically inspired propulsion systems for autonomous underwater vehicles *Proc. Inst. Mech. Eng.* M **225** 77–96

[51] Peraza-Hernandez E A, Hartl D J and Malak R J Jr 2013 Design and numerical analysis of an SMA mesh-based self-folding sheet *Smart Mater. Struct.* **22** 094008

[52] Gilewski W, Pełczyński J and Stawarz P 2014 A comparative study of origami inspired folded plates *Proc. Eng.* **91** 220–5

[53] Yu J *et al* 2016 Towards a miniature self-propelled jellyfish-like swimming robot *Int. J. Adv. Robotic Syst.* **13** 1–9

[54] Ren Z *et al* 2019 Multi-functional soft-bodied jellyfish-like swimming *Nat. Commun.* **10** 2703

[55] Berkooz G, Holmes P J and Lumley J 2003 The proper orthogonal decomposition in the analysis of turbulent flows *Annu. Rev. Fluid Mech.* **25** 539–75

[56] Masud A, Bhanabhagvanwala M and Khurram R A 2007 An adaptive mesh rezoning scheme for moving boundary flows and fluid-structure interaction *Comput. Fluids* **36** 77–91

[57] Chorin A J 1967 A numerical method for solving incompressible viscous flow problems *J. Comput. Phys.* **2** 12–26

[58] Meneghini J R, Saltara F, Siqueira C L R and Ferrari J A 2001 Numerical simulation of flow interference between two circular cylinders in tandem and side-by-side arrangements *J. Fluid Struct.* **15** 327–50

[59] Zhao M, Cheng L, Teng B and Dong G 2007 Hydrodynamic forces on dual cylinders of different diameters in steady currents *J. Fluid Struct.* **23** 59–83

[60] Brooks A N and Hughes T J R 1982 Streamline upwind/Petrov–Galerkin formulations for convection dominated flows with particular emphasis on the incompressible Navier–Stokes equations *Comput. Methods Appl. Mech. Eng.* **32** 199–259

[61] Choi H G, Choi H and Yoo J Y 1997 A fractional four-step finite element formulation of the unsteady incompressible Navier–Stokes equations using SUPG and linear equal-order element methods *Comput. Methods Appl. Mech. Eng.* **143** 333–48

[62] Bao Y, Zhou D, Huang C, Wu Q and Chen X-q 2011 Numerical prediction of aerodynamic characteristics of prismatic cylinder by finite element method with Spalart–Allmaras turbulence model *Comput. Struct.* **89** 325–38

[63] Wang H *et al* 2014 Wake-induced vibrations of an elastically mounted cylinder located downstream of a stationary larger cylinder at low Reynolds numbers *J. Fluid Struct.* **50** 479–96

[64] Shinde V *et al* 2019 Galerkin-free model reduction for fluid-structure interaction using proper orthogonal decomposition *J. Comput. Phys.* **396** 579–95

[65] Gray J 1953 The locomotion of fishes *Essays in Marine Biology* 1–16

[66] Borazjani I and Sotiropoulos F 2009 Numerical investigation of the hydrodynamics of anguilliform swimming in the transitional and inertial flow regimes *J. Exp. Biol.* **212** 576–92

[67] Ford M and Costello J 2000 Kinematic comparison of bell contraction by four species of hyromedusae *Sci. Mar.* **64** 47–53

[68] Borazjani I and Sotiropoulos F 2008 Numerical investigation of the hydrodynamics of carangiform swimming in the transitional and inertial flow regimes *J. Exp. Biol.* **211** 1541–58

[69] Hochreiter S and Schmidhuber J 1997 Long short-term memory *Neural Comput.* **9** 1735–80

[70] Goodfellow I, Bengio Y and Courville A 2016 *Deep Learning* (Cambridge, MA: MIT Press)

[71] Long J H, Koob T, Schaefer J, Summers A, Bantilan K, Grotmol S and Porter M 2011 Inspired by sharks: a biomimetic skeleton for the flapping, propulsive tail of an aquatic robot *Mar. Technol. Soc. J.* **45** 119–29

[72] Kingma D and Ba J 2014 Adam: a method for stochastic optimization *Int. Conf. Learning Representations*

[73] Bergmann M and Iollo A 2011 Modeling and simulation of fish-like swimming *J. Comput. Phys.* **230** 329–48

[74] Floryan D, Van Buren T and Smits A 2020 Swimmers' wake structures are not reliable indicators of swimming performance *Bioinspiration Biomimetics* **15** 024001

[75] Schultz W W and Webb P 2002 Power requirements of swimming: do new methods resolve old questions? *Integr. Comp. Biol.* **42** 1018–25

[76] Tytell E D and Lauder G V 2004 The hydrodynamics of eel swimming *J. Exp. Biol.* **207** 1825–41

[77] Lauder G 2014 Fish locomotion: recent advances and new directions *Ann. Rev. Mar. Sci.* **7** 521–45

[78] Jones K and Platzer M 1997 Numerical computation of flapping-wing propulsion and power extraction *AIAA* 97

[79] Costello J H and Colin S P 1994 Morphology, fluid motion and predation by the scyphomedusa Aurelia aurita *Mar. Biol.* **121** 327–34